

**FAST REGISTRATION OF CONTRAST-ENHANCED
MAGNETIC RESONANCE IMAGES OF THE BREAST**

SUN YIN

NATIONAL UNIVERSITY OF SINGAPORE

2007

FAST REGISTRATION OF CONTRAST-ENHANCED
MAGNETIC RESONANCE IMAGES OF THE BREAST

SUN YIN

(B.Eng (Hons.), NUS)

A THESIS SUBMITTED
FOR THE DEGREE OF MASTER OF ENGINEERING
DEPARTMENT OF ELECTRICAL & COMPUTER ENGINEERING
NATIONAL UNIVERSITY OF SINGAPORE

2007

Acknowledgments

Many people have given me their kind help in this work. I wish to express my heartfelt gratitude to my project supervisors Dr. Yan Chye Hwang and A/P. Ong Sim Heng. I am thankful for their unwavering support, generous guidance and kind encouragement throughout the course of this project. The discussions we had sparked many exciting new ideas for my research. I am grateful for the useful criticisms they have given me which greatly improved this work. I would like to thank A/P. Wang Shih Chang from the Department of Radiology as well. His invaluable help in the subjective evaluation of the results is greatly appreciated. I also feel fortunate to have my fellow labmates around who made my daily life in the lab fun and enjoyable. Last but not least, I thank my parents and Miss Wu Ying for supporting my decision of pursuing graduate studies. Hope that they can find joy in this achievement.

Sun Yin

March, 2007

Contents

Acknowledgments	i
List of Figures	vi
List of Tables	vii
Summary	viii
1 Introduction	1
1.1 Background	1
1.2 Motivation	5
1.3 Contributions	6
1.3.1 Registration Using Approximated NMI Gradient	6
1.3.2 Hardware Acceleration Using GPU	7
1.4 Organization of the Thesis	7
2 Image Registration	8
2.1 Overview	8
2.2 Problem Formulation	8
2.3 Transformation Models	9

2.3.1	Global Motion Model	10
2.3.2	Local Motion Model	11
2.4	Similarity Measure	12
2.5	Search Strategy	14
3	Fast Registration Using Approximated NMI Gradient	16
3.1	Overview	16
3.2	Method	17
3.2.1	Assumptions about Probability Density Functions	17
3.2.2	Estimating the Conditional PDF	17
3.2.3	Approximation of the NMI Gradient	18
3.2.4	Relation to Correlation Ratio	23
3.3	Study Design	24
3.3.1	Data	24
3.3.2	Implementation Details	24
3.3.3	Evaluation of Registration	25
3.4	Results and Discussion	27
3.4.1	Registration Quality	27
3.4.2	Effect on Lesion-Volume Reduction	28
3.4.3	Computational Complexity	31
3.5	Conclusion	33
4	A Framework for Registration Using GPUs	35
4.1	Introduction	35

4.2	Piece-wise Linear Transform and Optimization	37
4.3	GPU Implementation	39
4.3.1	Basics of GPU Programming	39
4.3.2	GPU-based Registration	40
4.4	Experiments and Results	46
4.4.1	Selection of Control Point Resolution	48
4.4.2	Registration Result on More Datasets	50
4.4.3	Analysis of Running Time	50
5	Conclusion	55
A	Derivation of NMI gradient	57
	Appendix: Derivation of NMI gradient	59
	Bibliography	59

List of Figures

1.1	An example slice from a typical dataset. Left: pre-contrast image, Right: post-contrast image. Substantial enhancement can be observed in the left breast lesion.	2
3.1	Plot of conditional PDF given the intensity in the pre-contrast image is 30 (including some tumor voxels before enhancement and some voxels of normal tissue). We can see that the intensity of the tumor voxels have increased to around 80 while the normal voxels have increased slightly to around 40.	19
3.2	Histogram plot of the rankings received by different registration methods for boundary registration. Rank 1 was assigned to the image with the best breast boundary registration.	29
3.3	Histogram plot of the rankings received by different registration methods for motion artifact reduction. Rank 1 was assigned to the image with the least amount of motion artifact.	30
3.4	A dataset with relatively small amount of motion. In this case, rigid and nonrigid registrations were rated similarly in the subjective tests. From left to right: Maximum Intensity Projection (MIP) subtraction (before registration), MIP subtraction (rigid NMI), MIP subtraction (rigid NMISD), MIP subtraction (nonrigid NMI), MIP subtraction (nonrigid NMISD).	31
3.5	A dataset with moderate amount of motion. In this case, nonrigid registration performed clearly better than rigid registration. From left to right: Maximum Intensity Projection (MIP) subtraction (before registration), MIP subtraction (rigid NMI), MIP subtraction (rigid NMISD), MIP subtraction (nonrigid NMI), MIP subtraction (nonrigid NMISD).	31

3.6	Lesion volume test Case 1. Top from left to right: Maximum Intensity Projection (MIP) subtraction (before registration), MIP subtraction (rigid NMI), MIP subtraction (rigid NMISSD), MIP subtraction (non-rigid NMI), MIP subtraction (nonrigid NMISSD). Bottom from left to right: binary lesion masks of the corresponding top row image. Non-rigid registration by NMI has caused the lesion to shrink by 22.63%, while NMISSD has reduced the shrinkage to 2.23%.	32
3.7	Lesion volume test Case 2. Top from left to right: Maximum Intensity Projection (MIP) subtraction (before registration), MIP subtraction (rigid NMI), MIP subtraction (rigid NMISSD), MIP subtraction (non-rigid NMI), MIP subtraction (nonrigid NMISSD). Bottom from left to right: binary lesion masks of the corresponding top row image. Non-rigid registration by NMI has caused the lesion to shrink by 8.71%, while NMISSD has reduced the shrinkage to 3.14%.	33
4.1	The graphics pipeline in latest generation graphics hardware. Programmable vertex and fragment processors provide added flexibility. .	39
4.2	Illustration of the data storage scheme. Slices of the 3D volume are packed into a single 2D flat texture.	41
4.3	The reduce operation to sum up the values in a texture.	43
4.4	2D illustration of the localized support of each control point. The points marked red are positioned alternately on the control point grid, and therefore the similarity measure gradients can be computed simultaneously for them. The region of support is also shown for one of the control point.	44
4.5	Block diagram of the GPU registration system.	47
4.6	Top left: Pre-contrast image. Top right: Post-contrast image. Bottom left: Maximum Intensity Projection (MIP) of the difference image before registration. Bottom right: MIP after GPGPU registration. . .	51
4.7	Top left: Pre-contrast image. Top right: Post-contrast image. Bottom left: Maximum Intensity Projection (MIP) of the difference image before registration. Bottom right: MIP after GPGPU registration. . .	52
4.8	Plot of running time in seconds against the image size.	54

List of Tables

3.1	Effect of lesion volume change before and after nonrigid registration. The size of lesion is given in mm ³ and percentage of changes in volume before and after registration by different methods are listed.	34
3.2	Registration timing for different methods.	34
4.1	Effect of varying control point resolution on the registration results. .	49
4.2	Effect of varying control point resolution on the registration results. .	54
4.3	Running time analysis for different image sizes.	54

Summary

Contrast-enhanced magnetic resonance (MR) imaging is an effective tool for the detection and analysis of female breast cancer. The imaging protocol consists of 3D volumes acquired at different times before and after the administration of a contrast agent. Intensity-time profiles are constructed for every voxel to aid in the diagnosis process. However, because of the voluntary or involuntary movements of the patients, the images have to be registered before a diagnosis can be reliably given.

Nonrigid deformation based on B-splines optimizing the normalized mutual information (NMI) criterion has proved to be successful in this registration task involving elastic deformations. In the first part of this work, we have proposed a fast approximation algorithm to estimate the gradient of NMI using a set of auxiliary images constructed from the image conditional probability distributions. Our method could speed up the registration process by an order of magnitude with similar registration quality. In the second part, we aimed to further speed up the registration process by offloading the bulk of the computational load to the GPU hardware for efficient processing. We exploited the single instruction multiple data (SIMD) processing capabilities and the dedicated interpolation hardware to obtain a further speed up of 15-30 times compared to CPU implementation.

Chapter 1

Introduction

1.1 Background

Contrast-enhanced magnetic resonance mammography (CEMRM) uses magnetic resonance imaging (MRI) to obtain the 3-D image of the human breast. A bolus injection of a contrast agent, usually a low molecular weight, freely diffusible molecule containing a chelate of gadolinium, is administered after an initial non-enhanced scan, and a series of T_1 -weighted images, typically using a 3-D gradient echo sequence, is acquired repeatedly at the same spatial location. The enhancement of the tissue by the contrast agent is acquired, and can be subsequently analyzed. One slice from an example dataset is shown in Figure 1.1.

The contrast agent is rapidly extracted from the intravascular compartment to the extracellular fluid space (or interstitial space) by a combination of perfusion and passive diffusion, which is in turn dependent on the microvascular density of the tissue, as well as tissue vascular permeability and the proportion of extracellular fluid

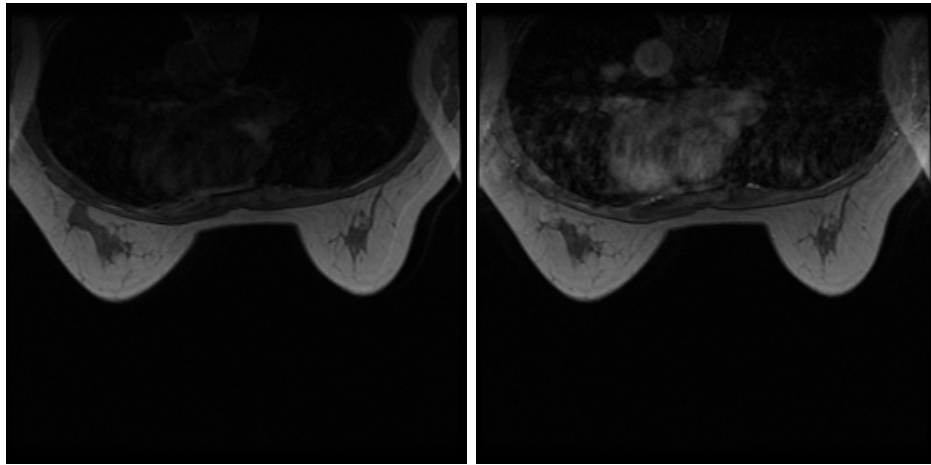


Figure 1.1. An example slice from a typical dataset. Left: pre-contrast image, Right: post-contrast image. Substantial enhancement can be observed in the left breast lesion.

space in the tissue. In the breast, all normal, non-fat tissues will exhibit contrast leakage and enhancement eventually. However, tissues with increased perfusion, microvascular density, capillary permeability, extracellular fluid space or a combination of any of these factors, will exhibit more rapid and intense enhancement than normal tissues. This increase in rate and degree of enhancement forms the foundation of breast MRI and its use to detect cancer and other pathologies [1].

In general, most cancers, infections and some benign processes such as fibroadenomas exhibit intense enhancement within 1-3 minutes after intravenous contrast injection, often with an initial rapid enhancement phase, while most benign lesions, very few cancers and normal breast tissue usually show slower, progressive and less intense enhancement over the first 5 minutes after injection. The terms “wash-in” and “wash-out” have been applied to the temporal enhancement of lesions and tissues in the breast after contrast injection. “Wash-in” refers to the initial contrast enhancement phase, while “wash-out” is normally only seen in the usual clinical imaging

timeframe of about 10 minutes after injection in lesions with a combination of high blood flow, high microvascular density and high vascular permeability, leading to contrast enhancement actually falling from an initial peak over the ensuing minutes. This finding is highly specific for malignant invasive cancers, and is rarely seen in benign processes or tissues. From the set of acquired images, we can construct a contrast enhancement timecourse curve for every voxel to estimate the enhancement and, if present, the wash-out rates, in order to classify the tissue. However, such analysis cannot always be directly applied since patient motion due to breathing and discomfiture is often present. The breast is also soft and deformable and will not move in a uniform fashion between acquisitions. Standard methods of image subtraction available in clinical MRI workstations do not use any formal registration scheme, and assume negligible patient motion between acquisitions. CEMRM offers better tissue sensitivity and 3-D tomography compared to x-ray mammography [2], and it is radiation-free. If registration can be made accurate and reliable, CEMRM can be more reliably applied for breast cancer detection.

Registration of contrast-enhanced breast MR images has been studied by several research groups. Many attempts employed mutual information (MI) or normalized mutual information (NMI) as a similarity measure [3, 4, 5, 6, 7]. MI was proposed independently by Collignon *et al.* [8] and Viola *et al.* [9]. To reduce the sensitivity of MI to image overlap, normalized mutual information (NMI) was proposed by Studholme *et al.* [10]. MI and NMI measure the statistical dependency between pairs of images and are therefore insensitive to intensity changes.

Rueckert *et al.* [7] showed that free-form deformation is a viable tool to effec-

tively reduce the motion artifacts that exist in CEMRM images. They proposed a combination of global affine and local free-form transformation to model the image deformation. It was demonstrated that most of the motion artifacts could be eliminated during the non-rigid local registration phase. Although free-form deformation could reduce motion artifacts, if it is performed in an unconstrained fashion, there would be artificial volume reduction of contrast-enhanced lesions due to intensity changes [6]. This is definitely undesirable since breast tissue is known to be almost incompressible. Furthermore, this side-effect may lead to an apparent reduction in enhancement for small lesions, reducing their conspicuity and potentially causing diagnostic errors. Currently, the problem of lesion volume reduction is addressed by adding a regularization term to the cost function. Rueckert *et al.* used a smoothness constraint on the transformation to control its “bending energy”. Rohlfing *et al.* [5] have proposed an incompressibility constraint based on the Jacobian of the transformation function. The Jacobian-based regularization penalizes both local contraction and expansion of the transformation, then favoring volume-preserving transformations. Rohlfing *et al.* have also suggested in [11] that when an over-constrained optimization is stuck in a local minimum, some of the artifacts are not removed as a result. A good solution would be to relax the constraint and allow it to escape from the local minimum.

Haber [12] addressed the problem of volume preservation using constrained registration with regularization, and the solution was found using sequential quadratic programming (SQP). Chen *et al.* [13] solved the problem by simultaneous segmentation and registration in an unified Bayesian framework. In particular, they have integrated a pharmacokinetic model into a hidden markov model (HMM) framework

for the segmentation step. Segmentation and registration are performed alternately until convergence. In order to make sure that nonrigid registration using FFD and NMI with incompressibility constraint is accurate, Tanner *et al.* [14] presented validation studies using finite element model (FEM), and the results confirmed the reliability of the method.

The calculation of MI and NMI is a highly computationally intensive task. It requires the formation of the joint histogram of corresponding voxel pairs. The optimization of the transformation parameters often requires computation of the gradient of the MI- or NMI-based cost function with respect to the transformation parameters. With appropriate interpolation of the histogram, an analytic expression can be computed for MI derivatives. Maes *et al.* [15] used partial volume interpolation on the histogram and derived analytic derivatives of MI to allow exact computation of the gradient. Thévenaz *et al.* [16] used Parzen windowing to form the histogram and derived an analytic form for the MI gradient. Computing the gradient may also be done by numerical approximation, e.g., a stochastic approximation [17], or a finite-difference approximation [3]. Stochastic approaches have the advantage of using a subset of the data set, thus reducing the computational complexity.

1.2 Motivation

A fast registration method is desirable in a clinical setting. Since motion recovery process is a typical *ill-posed* problem, we need to employ an optimization approach to solve it. Many optimization techniques such as gradient descent, conjugate gradient, and Levenberg-Marquardt(LM) require the gradient information in the search

process. To effectively compute the gradient of the cost function is therefore very useful. In this thesis, we describe an approach that reduces the complexity of NMI gradient computation by approximation. We have also observed that the commodity graphics processing unit (GPU) has gained attention in recent years as a cheap yet powerful computational resource. We attempt to exploit its dedicated hardware for image processing operations to further speed up the system.

1.3 Contributions

With the aim of achieving fast registration of CEMRM images, we have made contributions in the following areas.

1.3.1 Registration Using Approximated NMI Gradient

We observe that the conditional PDF of voxel intensities belonging to fatty and glandular tissues in two images can be approximated by a Gaussian function, and the enhanced structures by another Gaussian function with an increased mean value. If we do not make a distinction between tissue types, the combined conditional PDF of voxel intensities in the two images will be modeled by a mixture of Gaussians because tissues of different types might possess similar intensities. By doing so, we can approximate the gradient of NMI by the gradients of two SSD terms involving auxiliary images and the original images. The SSD gradients can be computed efficiently using finite difference approximation.

1.3.2 Hardware Acceleration Using GPU

We observe that the transformation and interpolation processes contribute to the bulk of the computational load, and that the local support of the B-splines provides a natural structure for parallelized processing. In the second part of this work, we propose a framework to perform registration on off-the-shelf commodity graphics processing unit (GPU). We describe the design and implementation of a parallel scheme which fully utilizes the single instruction multiple data (SIMD) architecture on GPU to optimize the control points in parallel. The dedicated graphics processing hardware for interpolation is exploited to further shorten the computation time.

1.4 Organization of the Thesis

In Chapter 2, we give an overview of the several components in the general registration framework. We review the techniques that are currently in use. In Chapter 3, we present the details of the approximated NMI gradient method that can greatly simplify and speed up the registration process. In Chapter 4, a method to utilize commodity graphics processing units to speed up the registration system is presented, and we conclude the thesis in Chapter 5.

Chapter 2

Image Registration

2.1 Overview

In this chapter, we describe how the registration problem is formulated in the current literature. The formulation can be separated into three modules: the transformation, the similarity measure and the optimizer. A short description of each component is given in the subsequent sections.

2.2 Problem Formulation

Image registration is the process of finding a transformation between a pair of images. We consider the pre-contrast image to be the reference image and denote it by u . The post-contrast image is to be mapped onto the pre-contrast image and it is denoted by v , where $\{u, v : \mathbb{R}^3 \mapsto \mathbb{R}\}$ are functions that maps the image voxels to intensities. Since all the images used in this work are in digitized form, we only consider a discrete coordinate grid and denote it as \mathbf{x} . $T(\cdot)$ defines some geometrical transformation that

models the motion between images. Defining some similarity measure $S(\cdot)$ that is optimized when the images are well aligned, we formulate the overall registration as

$$T = \arg \max_T (S(u(\mathbf{x}), v(T(\mathbf{x}))) \quad (2.1)$$

The optimal transformations will be given by the function T that optimizes S , which could be any similarity measure that measures registration quality.

2.3 Transformation Models

Transformations define mappings from one image to another, and they are controlled by its parameters. The ability of a transformation to model complex deformations is determined by its degree of freedom, or the number of independent parameters. Examples of transformations with low degree of freedom are affine, rigid and similarity transforms. Transformations with high degree of freedom often are defined using basis functions. A good example is freeform deformation based on B-splines. In this project, we have adopted a coarse to fine matching strategy similar to [7]. An initial global coarse matching is first achieved using rigid transformation, followed by a local motion correction using freeform deformation.

$$T(\mathbf{x}) = T_{global}(\mathbf{x}) + T_{local}(\mathbf{x}) \quad (2.2)$$

2.3.1 Global Motion Model

We have chosen to use rigid transform to model the global motion. Consider a point (x, y, z) in the coordinate grid \mathbf{x} , the rigid transform is given by

$$T_{global}(x, y, z) = \mathbf{R}(x, y, z) + \mathbf{T} \quad (2.3)$$

where \mathbf{R} is a matrix representing a rotation and \mathbf{T} is a matrix representing a translation.

If we denote the angle rotated about the x -axis by α , the angle rotated about the y -axis by β and the angle rotated about the z -axis by γ , we can write \mathbf{R} in the following form,

$$\mathbf{R} = \mathbf{R}(\alpha)\mathbf{R}(\beta)\mathbf{R}(\gamma) \quad (2.4)$$

where $\mathbf{R}(\alpha)$, $\mathbf{R}(\beta)$ and $\mathbf{R}(\gamma)$ are given respectively by

$$\mathbf{R}(\alpha) = \begin{pmatrix} 1 & 0 & 0 \\ 0 & \cos \alpha & -\sin \alpha \\ 0 & \sin \alpha & \cos \alpha \end{pmatrix} \quad (2.5)$$

$$\mathbf{R}(\beta) = \begin{pmatrix} \cos \beta & 0 & \sin \beta \\ 0 & 1 & 0 \\ -\sin \beta & 0 & \cos \beta \end{pmatrix} \quad (2.6)$$

$$\mathbf{R}(\gamma) = \begin{pmatrix} \cos \gamma & -\sin \gamma & 0 \\ \sin \gamma & \cos \gamma & 0 \\ 0 & 0 & 1 \end{pmatrix} \quad (2.7)$$

The translation matrix \mathbf{T} is given by

$$\mathbf{T} = \begin{pmatrix} t_x \\ t_y \\ t_z \end{pmatrix} \quad (2.8)$$

2.3.2 Local Motion Model

In this section, we describe the local motion model that we employed. Rigid transformation only removes the global motion between the images. Since the breast is soft, it is easy to find nonrigid deformation where a global mapping is insufficient. Freeform deformation using B-splines has been proved to be a powerful method to be used in modeling deformable objects. The idea of freeform deformation is to use an uniformly spaced grid of control points to represent local displacements, and to use B-spline interpolation to find the displacement vectors for the voxels in between the control points. Every control point is to be moved independently in 3D space, thus deforming the image volume.

To represent freeform deformation, we define a grid of control points Φ with dimension $n_x \times n_y \times n_z$ and we use $\phi_{a,b,c}$ to denote one particular control point. The control point spacing in different axis directions are denoted by $\{\delta_x, \delta_y, \delta_z\}$. Then 3D free-form deformation is given by a tensor product of 1D B-splines,

$$T_{local}(x, y, z) = \sum_{l=0}^3 \sum_{m=0}^3 \sum_{n=0}^3 B_l(d_x) B_m(d_y) B_n(d_z) \phi_{a+l, b+m, c+n} \quad (2.9)$$

where $a = \lfloor x/n_x \rfloor - 1$, $b = \lfloor y/n_y \rfloor - 1$ and $c = \lfloor z/n_z \rfloor - 1$. $\{d_x, d_y, d_z\}$ denotes distance

of the voxel to its neighbor control point and they are given by $d_x = x - \lfloor x/\delta_x \rfloor$, $d_y = y - \lfloor y/\delta_y \rfloor$ and $d_z = z - \lfloor z/\delta_z \rfloor$, where $\lfloor \cdot \rfloor$ is the floor operation.

The B-spline basis functions are given by

$$B_0(t) = (1 - t)^3/6 \quad (2.10)$$

$$B_1(t) = (3t^3 - 6t^2 + 4)/6 \quad (2.11)$$

$$B_2(t) = (-3t^3 + 3t^2 + 3t + 1)/6 \quad (2.12)$$

$$B_3(t) = t^3/6 \quad (2.13)$$

Since the displacement vector of a voxel is interpolated from its immediate $4 \times 4 \times 4$ neighborhood of control points, moving one control point only affects a local support of the image. This nice property permits efficient computation of the transformation. In 3 dimensional space, each control point has 3 degrees of freedom. For a $10 \times 10 \times 10$ grid of control points, we have a transformation with 3000 degree of freedom. Comparing to rigid transform, there is a enormous increase of degree of freedom and it allows efficient modeling of deformable objects. However, large number of control points demand substantial computation time. In practice, it is needed to consider the tradeoff between time and accuracy when deciding the number of control points to use.

2.4 Similarity Measure

Similarity measures are defined to give a quantitative indication of how well two images resemble one another. They are usually defined to be a function which gives

a single numerical output.

One of the simplest similarity measure will be the SSD criterion,

$$\text{SSD}(u, v) = \sum_k [u(\mathbf{x}_k) - v(T(\mathbf{x}_k))]^2 \quad (2.14)$$

We have used \mathbf{x}_k to denote every possible voxels (indexed by k) in the coordinate grid. The SSD criterion is attractive because of its low complexity, but its direct application to this problem is not possible because of the non-uniform change in intensity. If we wish to use SSD criterion, we first have to correct for this.

Information-theoretic measures do not require the two images to have the same intensity range. Mutual information (MI) and normalized mutual information (NMI) falls into this category. MI is defined as

$$\text{MI}(u, v) = H(u(\mathbf{x})) + H(v(T(\mathbf{x}))) - H(u(\mathbf{x}), v(T(\mathbf{x}))) \quad (2.15)$$

and NMI is defined as

$$\text{NMI}(u, v) = \frac{H(u(\mathbf{x})) + H(v(T(\mathbf{x})))}{H(u(\mathbf{x}), v(T(\mathbf{x})))} \quad (2.16)$$

where $H(u(\mathbf{x}))$ and $H(v(\mathbf{x}))$ denote the marginal entropies (ME) and $H(u(\mathbf{x}), v(T(\mathbf{x})))$ the joint entropy (JE). We can calculate the entropy terms from the joint histogram in terms of discrete intensity values. If we denote the number of bins in the histogram by I and J , the number of entries in i th row and j th column by n_{ij} and the total

number of entries by N , we have

$$\begin{aligned}
 H(u(\mathbf{x})) &= - \sum_{i \in I} p(i) \log(p(i)) \\
 H(v(T(\mathbf{x}))) &= - \sum_{j \in J} p(j) \log(p(j)) \\
 H(u(\mathbf{x}), v(T(\mathbf{x}))) &= - \sum_{i \in I} \sum_{j \in J} p(i, j) \log(p(i, j))
 \end{aligned} \tag{2.17}$$

where $p(i) = \sum_j n_{ij}/N$, $p(j) = \sum_i n_{ij}/N$ and $p(i, j) = n_{ij}/N$.

Both MI and NMI measures the similarity of images from their statistical dependencies in intensities. They do not require the structures in different images to possess exactly the same intensities. But as optimization process proceeds, they build up their own intensity matching restrictions and seek for an optimum which minimizes JE. NMI is said to be the "normalized" version of MI because the fact that it is insensitive to the amount of overlap in the images. And this facilitates the optimization process because its value subjects to less fluctuations.

2.5 Search Strategy

Since we have formulated image registration as an optimization problem, we need to search for the optimal parameters which give the best similarity measure. Theoretically, an exhaustive search which guarantees global optimum would be ideal. However, it is infeasible due to the large number of parameters and the wide range of possible values that the parameters can take.

In practice, we usually employ intelligent strategies and only search a fraction of

the search space in order to save time. The search strategies can be broadly divided into two categories: gradient based and non-gradient based. Methods like simplex, Powell's direction set and evolutionary strategies like genetic algorithm all fall into the category of non-gradient based methods. For gradient based methods, we usually first compute the gradient of the similarity measure, then search for the optimal parameter along the direction of the gradients.

In this project, we have chosen to use gradient-based techniques due to its nice convergence properties and simplicity in implementation. Since we usually have good initialization for the image datasets we have, the local optimum found by gradient-based techniques such as the gradient descent is sufficiently good.

Chapter 3

Fast Registration Using Approximated NMI Gradient

3.1 Overview

We describe in this chapter an intensity-based registration algorithm for the analysis of contrast-enhanced breast MR images [18][19]. Motion between pre-contrast and post-contrast images is modeled by a combination of rigid transformation and free-form deformation. We propose a fast method to compute an approximation of the gradient of normalized mutual information (NMI) by the use of intensity-corrected auxiliary images. The registration time can be reduced by 50% with comparable performance. One well-known problem of non-rigid registration of contrast enhanced images is the contraction of enhanced lesion volume. By modeling the outliers explicitly in the computation of similarity measure, we can effectively prevent artificial volume reduction.

3.2 Method

3.2.1 Assumptions about Probability Density Functions

It has been shown that the joint probability density function (PDF) of the image voxel pairs can be modeled as a mixture of joint Gaussians [20]. The computational complexity of estimating the joint Gaussian mixtures is high due to the large number of parameters. We observe that in contrast enhanced MR mammography, the intensities of voxels change according to the different rates of contrast agent intake. For the voxels belonging to tissue types such as fatty and glandular which do not take in contrast agents, the intensities remain almost unchanged. If the initial alignment of the images is close, most of the voxels should match to voxels of the same tissue type and we expect to find similar intensities. Therefore, instead of modeling the joint probability function, we model the conditional probability density function between image voxel pairs contributed by the non-enhanced structures by a Gaussian. For the enhanced structures, we expect the intensities of corresponding voxels found in the post-contrast image to be brighter. Because the amount of intensity changes are dependent on the rates of contrast agent uptake, we model them using another Gaussian distribution with a different mean value.

3.2.2 Estimating the Conditional PDF

Given one intensity u from the pre-contrast image, we take the column $i = u$ from the joint histogram to estimate the conditional means and variances. The histogram bins in the dimension j are considered as outliers if $j - i > \omega$, where ω is a threshold. That

means the corresponding voxel contains significant enhancement and the intensity has increased greatly.

The threshold value is estimated from the histogram. Given an intensity $u = i$ in the pre-contrast image, we assume that the outlier intensities is always greater than the given intensity, and the inlier conditional means should be close to the given intensity i . Therefore, we use the histogram bins where $j < i$ to estimate the conditional variance σ assuming the conditional mean is equal to i , and set $\omega = i + 3\sigma$. If given an intensity $v = j$ from the post-contrast image, the outlier should have an intensity smaller than the given intensity and the threshold is determined as $\omega = j - 3\sigma$, where σ is estimated using histogram bins $i > j$.

We show in Figure 3.1 an example plot of the conditional PDF obtained from our test data sets. The means and variances for the inliers and outliers are estimated respectively. We have shown in the plot the raw histogram data, the Gaussian curves estimated and the combined mixture of Gaussians. We can see that the estimated Gaussian functions fit the data well. Motivated by this observation, we derive an approximation to the NMI gradients in the next subsection.

3.2.3 Approximation of the NMI Gradient

In the optimization process, it is often required to compute its gradient with respect to a transformation. For the pair of voxels $u(\mathbf{x}_k)$ and $v(T(\mathbf{x}_k))$ indexed at \mathbf{x}_k , we denote the former simply by u_k and the latter by v_k^T to denote the dependence on the mapping T . As described in the appendix, the gradient of NMI with respect to

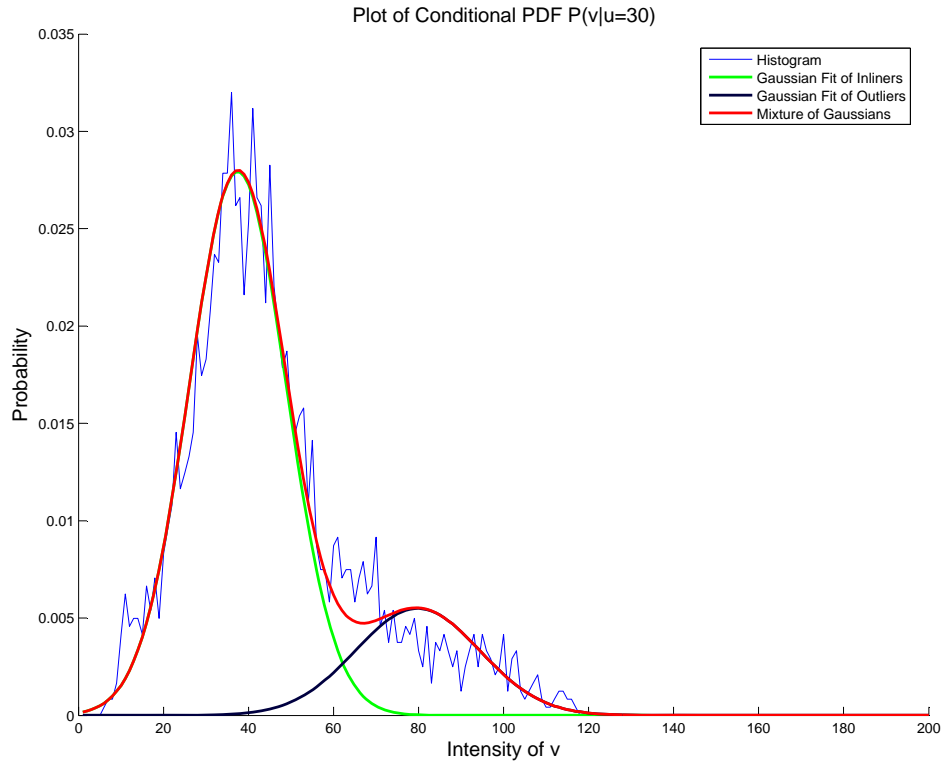


Figure 3.1. Plot of conditional PDF given the intensity in the pre-contrast image is 30 (including some tumor voxels before enhancement and some voxels of normal tissue). We can see that the intensity of the tumor voxels have increased to around 80 while the normal voxels have increased slightly to around 40.

a transformation parameter can be written as,

$$\frac{\partial \text{NMI}(u, v^T)}{\partial \phi} \simeq \frac{1}{H^2(u, v^T)} \left[-\text{MI}(u, v^T) \frac{\partial H(v^T|u)}{\partial \phi} - H(u, v^T) \frac{\partial H(u|v^T)}{\partial \phi} \right] \quad (3.1)$$

where $\text{MI}(u, v^T) = H(u) + H(v^T) - H(u, v^T)$ denotes the mutual information of the two images. $H(u|v^T)$ can be calculated from the joint histogram of the images formed

using the current mapping T .

$$H(u|v^T) = - \sum_{i \in I} \sum_{j \in J} p(i, j) \log(p(i|j)) \quad (3.2)$$

where $p(i, j) = n_{ij}/N$ and $p(i|j) = n_{ij} / \sum_j n_{ij}$. If we perform the summation over the set of all voxel positions \mathbf{x}_k , it can be rewritten as

$$H(u|v^T) = - \frac{1}{N} \sum_k \log(p(u_k|v_k^T)) \quad (3.3)$$

We model the conditional probability density function (conditional PDF) relating every possible image voxel intensity pairs using a mixture of standard Gaussians. The expression of the conditional PDF is given by

$$p(u_k|v_k^T) = p(u_k|v_k^T, \Omega_1)P(\Omega_1) + p(u_k|v_k^T, \Omega_2)P(\Omega_2) \quad (3.4)$$

where Ω_1 and Ω_2 denote the sets of inlier and outlier voxels respectively. Assuming that the conditional PDF is given by a mixture of standard Gaussian density functions, it leads to

$$\begin{aligned} p(u_k|v_k^T, \Omega_1) &= \frac{1}{\sqrt{2\pi}\sigma_{v_k^T, \Omega_1}} \exp\left(-\frac{(u_k - m_{v_k^T, \Omega_1})^2}{2\sigma_{v_k^T, \Omega_1}^2}\right) \\ p(u_k|v_k^T, \Omega_2) &= \frac{1}{\sqrt{2\pi}\sigma_{v_k^T, \Omega_2}} \exp\left(-\frac{(u_k - m_{v_k^T, \Omega_2})^2}{2\sigma_{v_k^T, \Omega_2}^2}\right) \end{aligned} \quad (3.5)$$

The parameters for every possible voxel intensity pair are different and should be estimated separately. The conditional means and variances can be estimated using

the method described in the previous section. Note that this estimation is only performed once every iteration.

We consider the mixing proportions $P(\Omega_1)$ and $P(\Omega_2)$ to be approximately constant with respect to transformation. The derivative with respect to a transformation parameter ϕ is

$$\begin{aligned} \frac{\partial}{\partial \phi} H(u|v^T) = & \frac{1}{N} \sum_k \frac{1}{p(u_k|v_k^T)} [p(u_k|v_k^T, \Omega_1)P(\Omega_1) \frac{\partial}{\partial \phi} \frac{(u - m_{v_k^T, \Omega_1})^2}{2\sigma_{v_k^T, \Omega_1}^2} \\ & + p(u_k|v_k^T, \Omega_2)P(\Omega_2) \frac{\partial}{\partial \phi} \frac{(u - m_{v_k^T, \Omega_2})^2}{2\sigma_{v_k^T, \Omega_2}^2}] \end{aligned} \quad (3.6)$$

Thus, we have the gradient of the total conditional entropy expressed in terms of a weighted combination of the gradient of two squared difference terms:

$$\begin{aligned} \frac{\partial}{\partial \phi} H(u|v^T) = & \frac{1}{N} \frac{\partial}{\partial \phi} \sum_k [w_{v_k^T, \Omega_1} (u_k - m_{v_k^T, \Omega_1})^2 + w_{v_k^T, \Omega_2} (u_k - m_{v_k^T, \Omega_2})^2] \\ = & \frac{1}{N} \frac{\partial}{\partial \phi} \text{WSSD}(u, w_{v^T, \Omega_1}, w_{v^T, \Omega_2}, m_{v^T, \Omega_1}, m_{v^T, \Omega_2}) \end{aligned} \quad (3.7)$$

where the weights for the inliers and outliers are given, respectively, by

$$\begin{aligned} w_{v_k^T, \Omega_1} &= \frac{p(u_k|v_k^T, \Omega_1)P(\Omega_1)}{2\sigma_{v_k^T, \Omega_1}^2 p(u_k|v_k^T)} \\ w_{v_k^T, \Omega_2} &= \frac{p(u_k|v_k^T, \Omega_2)P(\Omega_2)}{2\sigma_{v_k^T, \Omega_2}^2 p(u_k|v_k^T)} \end{aligned} \quad (3.8)$$

The weight images and the conditional means images for every voxel are updated at the start of every iteration using the current estimate of transformation. We can easily compute the WSSD gradient so as to obtain an approximation of the direction of the NMI gradient in the parameter search space. We can infer from the weighting

function: if the voxel pair belongs to the inlier set Ω_1 , the weights will be large for the first term. If the voxel pair belongs to the outlier set Ω_2 , the weight is smaller for the first term and larger for the second term. If we consider the summation of the WSSD voxel by voxel, there is one dominant term at every voxel depending on the class of the voxel. Similarly, we can derive another expression for $H(v^T|u)$ and the corresponding auxiliary images. It follows that an approximation of the NMI gradient with respect to a transformation variable ϕ is given by

$$\begin{aligned} \frac{\partial \text{NMI}(u, v^T)}{\partial \phi} \simeq & \frac{1}{NH^2(u, v^T)} \left[-\text{MI}(u, v^T) \frac{\partial}{\partial \phi} \text{WSSD}(v^T, w_{u, \Omega_1}, w_{u, \Omega_2}, m_{u, \Omega_1}, m_{u, \Omega_2}) \right. \\ & \left. - H(u, v^T) \frac{\partial}{\partial \phi} \text{WSSD}(u, w_{v^T, \Omega_1}, w_{v^T, \Omega_2}, m_{v^T, \Omega_1}, m_{v^T, \Omega_2}) \right] \end{aligned} \quad (3.9)$$

In (3.9), we see that the two WSSD terms involved are weighted by MI and JE respectively. At the initial stage of registration, JE will be large and MI small because the two images are not well aligned. Therefore, the value of the gradient will be dominated by the second WSSD term. With better alignment, we expect JE to decrease and MI to increase. The contributions of the two WSSD terms will be weighted accordingly.

In every iteration of the registration, we first construct the global joint histogram using the current estimate of the transformation. We then use the histogram bins with intensity range within the threshold value to compute the conditional means and variances, as well as the current estimate of MI and JE. We then proceed to construct the auxiliary images and estimate the direction of the NMI gradient. The auxiliary images are constructed only once per iteration and the time needed for its construction is negligible. Since our method modifies the traditional SSD and has an

additional NMI flavor, we call it NMISD.

3.2.4 Relation to Correlation Ratio

The correlation ratio (CR) was introduced by Roche *et al.* [21] as a registration similarity measure. It is derived from probability theory to measure the degree of similarity of two images. CR is expressed as

$$\eta(v|u) = \frac{\text{var}[E(v|u)]}{\text{var}(v)} \quad (3.10)$$

Its value ranges from 0 (least aligned) to 1 (well aligned). It is shown in [21] that

$$1 - \eta(v|u) = \frac{1}{N\sigma^2} \text{SSD}(u, m_v) \quad (3.11)$$

where N is the total number of voxel pairs, σ^2 is the variance of v , and m_v is the image formed from the conditional expectation $E(v|u)$. This expression is minimized in registration. It is interesting to note that our SSD computation is in fact similar to the computation of the correlation ratio, except for the fact that we have used two conditional means from a Gaussian mixture. The existence of equivalence provides new insights into the different similarity measures used. The derived expression of NMI gradient (3.9) combines MI, JE and CR in an elegant manner.

3.3 Study Design

3.3.1 Data

We used a total of 15 patient datasets obtained from the National University Hospital, Singapore. Out of the datasets, 8 breasts contain lesion and 22 breasts are normal. Image acquisition was done using a GE Sigma 1.5 Tesla coil MRI scanner with 3-D fast-spoiled gradient echo and no spectral fat suppression ($TR = 25.6\text{ms}$, $TE=3\text{ms}$, fractional echo, flip angle = 30° , $FOV = 32$ to 40cm). The contrast agent used was MagneVist Gd-DTPA of concentration 0.2mmol/kg . A typical data set has 5 scans ($256 \times 256 \times 24$ voxels) of voxel size $1.05\text{mm} \times 1.05\text{mm} \times 5.45\text{mm}$. Slice direction is axial. Variations to this protocol are mainly in the number of slices, which can vary from 16 to 56 depending on the volume size to be acquired, and the slice thickness, which depend on the size of the breast to be imaged. The contrast agent is injected after the first scan, with post-contrast scans in the next 5 to 20 minutes. Each 3-D scan requires 30-60 seconds of acquisition time.

3.3.2 Implementation Details

We have implemented the registration algorithm using C++. In our experiments, we manually defined a rectangle region of interest (ROI) around each breast from the maximum intensity projection (MIP) of the pre-contrast image in the axial direction. The same ROI was used for both pre-contrast and post-contrast images. ROI registration was performed using rigid registration followed by nonrigid registration based on B-spline basis functions. The transformation parameters were optimized

by gradient descent. The gradients of the two SSD terms in NMISD were approximated using finite differences, and the NMI gradient was approximated from them. Optimization was terminated when the change in cost function was smaller than a predefined threshold value. We have found that a threshold between 10^{-2} to 10^{-4} could achieve good registration. Nonrigid registration was performed employing a two level strategy using control points of two different resolutions. Due to the small ROI size (typically 100×100 mm with different number of slices), we kept the image resolution fixed. During registration, a coarse control point grid was applied first, then the control point resolution was halved by inserting new points to form a fine grid similar to Rueckert's method [7]. The displacements of the new points were interpolated from the old points using the same B-spline basis functions. We did not use any regularization in registration. When optimizing the control points, we took advantage of the compact local support of the B-spline basis functions and only computed the similarity measure using the affected voxels in the $4 \times 4 \times 4$ control point neighborhood. All the B-spline basis functions were pre-computed to further save time. When warping the template image, the interpolation method we used was tri-linear. In the estimation of the conditional means, we have used 50 bins in both dimensions of the joint histogram.

3.3.3 Evaluation of Registration

Subjective Test

It is difficult to provide a quantitative evaluation of the proposed nonrigid registration algorithm without available ground truth data. We thus resolved to subjective

evaluation of the registration results. We have registered the datasets using rigid and nonrigid registrations, using NMI and NMISD respectively as a similarity measure. The subtraction images were obtained and the results of the same dataset using different methods were blindly presented to an expert radiologist in a random order. The evaluation was performed slice by slice on the quality of breast boundary registration and the quality of motion artifact removal. For boundary registration, we specifically looked at how well the boundaries of the registered breast matched the original image in every slice of the subtraction image. For artifact reduction, we looked at the amount of interior motion artifacts present before and after registration. To compare the registration quality of different registration methods, we employed a ranking scheme. For every dataset, we obtained 4 sets of subtraction images from the registered images (NMI Rigid, NMISD Rigid, NMI Nonrigid, NMISD Nonrigid) and the subtraction images without registration. The radiologist ranked the results on breast boundary registration and artifact removal respectively. If the registration quality of two methods were indistinguishable, a tied ranking could be used.

Lesion Preservation

Since local contraction of the transformation is possible, we investigated the extent of volume contraction by different methods. To calculate the volume of the lesion, we manually created a binary mask of the breast lesion after rigid registration with lesion voxels assigned an intensity value of 255. A lesion was identified from the subtraction image after rigid registration. The volume of the lesion was determined from the total number of voxels in the mask that are labeled as lesion. To see whether there are

any changes in the lesion volume, we applied the final transformation obtained from the optimization process to the mask and compute the lesion volume in terms of the number of lesion voxels after transformation. Those voxels with interpolated intensities below 255 was considered to have contributed a fraction of voxel to the total lesion volume, so as to account for partial volume effect.

3.4 Results and Discussion

3.4.1 Registration Quality

The results for the visual inspection are shown in Figure 3.2 and Figure 3.3. From the distribution of the rankings, we can see that NMI and NMISD performed similarly for both rigid and nonrigid registration. For both boundary registration and artifact reduction test, nonrigid registration ranks better than or equal to rigid registration in most of the cases. For boundary registration, nonrigid registration using NMISD performed best (21, 6, 3, 0)¹. Nonrigid registration using NMI as a similarity measure also performed well (16, 9, 5, 0). Rigid registration generally received lower rankings with (5, 3, 18, 4) for NMISD and (5, 4, 15, 6) for NMI. For artifact reduction, non-rigid registration using NMISD performed well (23, 3, 4, 0). Nonrigid registration using NMI have received ranking (19, 7, 4, 0). Rigid registration using NMISD have received (9, 6, 8, 7) and rigid registration using NMI have received (10, 5, 8, 7).

Although nonrigid registration generally performed better than rigid registration for both tests, we note some exceptions in the rankings that in some cases rigid

¹21 cases assigned rank 1, 6 cases assigned rank 2, 3 cases assigned rank 3, 0 case assigned rank 4

registration received rankings 1 or 2. This is because in those test cases, the amount of motion are typically minor and nonrigid registration provided relatively small improvement over rigid registration. We have shown in Figure 3.4 one such case. In this case, nonrigid registration using NMI and NMISD all received rank 1 for both boundary registration and artifact reduction. However, since the motion is small and the quality of rigid registration using NMI and NMISD are acceptable too. They both received rank 1 for artifact reduction and rank 3 for boundary registration. We have also shown an example in Figure 3.5 where nonrigid registration clearly outperformed rigid registration. In this case, nonrigid registration using NMISD received rank 1 for both test, nonrigid registration using NMI received rank 2 for boundary registration and rank 1 for artifact reduction. Rigid registration using NMI and NMISD in this case all received rank 3 for both tests.

3.4.2 Effect on Lesion-Volume Reduction

In this section, we show results from tests on lesion volume reduction when nonrigid registration is used. In areas of strong intensity differences caused by the uptake of the contrast agent, misregistration will occur, resulting in the reduction of the volume of contrast enhancement. Due to image normalization, the intensity difference between the auxiliary and original images is smaller than the direct intensity difference between the original images. Ideally, if our normalization could remove all the intensity differences, there should not be any reduction in volume. However, the intensity

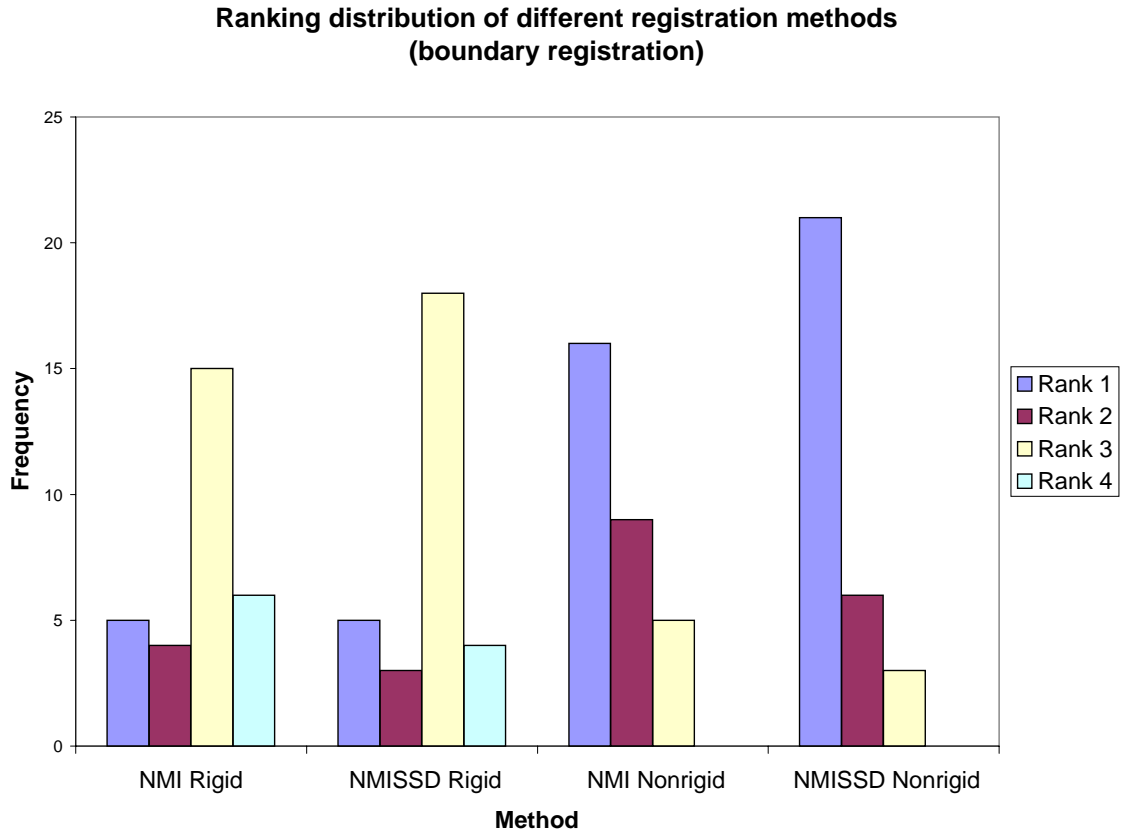


Figure 3.2. Histogram plot of the rankings received by different registration methods for boundary registration. Rank 1 was assigned to the image with the best breast boundary registration.

difference in the lesion region is too large and some of it is not removed by normalization. Hence, we still observe some volume reduction when registration is performed using NMISSD. In our experiments, the lesion datasets contain lesions of various sizes and we have tested the effect of nonrigid registration on volume changes. The lesion volume changes are evaluated using a control point grid with spacing 5mm. The registration was performed in an unconstrained manner. The results have been summarized in Table 3.1. It is generally observed that registration gives volume change after nonrigid registration. Due to the normalization of intensity, smaller amount

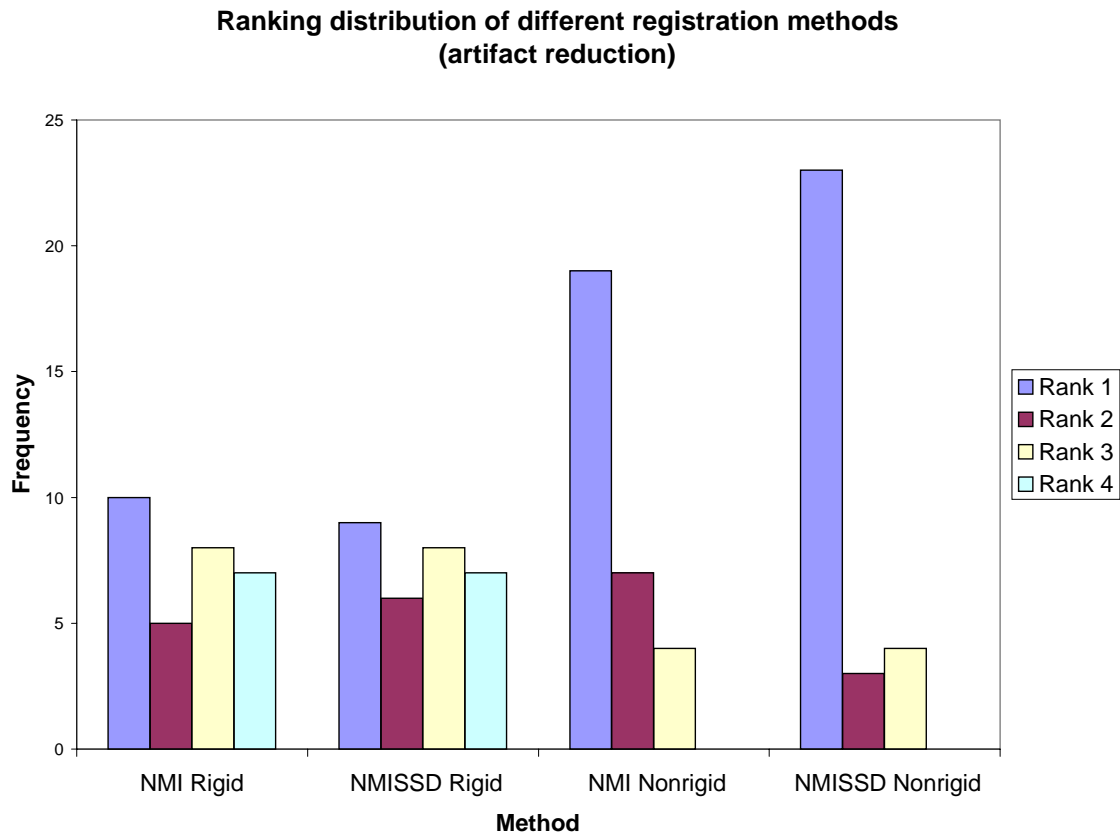


Figure 3.3. Histogram plot of the rankings received by different registration methods for motion artifact reduction. Rank 1 was assigned to the image with the least amount of motion artifact.

of volume change is observed with NMISSD. The creation of auxiliary images by NMISSD could remove some intensity changes in the non-lesion areas, thus reducing the possibility of local misregistration.

The maximum intensity projection (MIP) of Case 1 (Table 3.1) is shown in Figure 3.6. It can be seen that significant motion artifacts are present in the subtraction image without registration. With rigid registration, most of the artifacts are removed and the lesions are better visualized. After nonrigid registration, most of the artifacts are also removed, but the lesion volume is reduced and the shrinkage can be

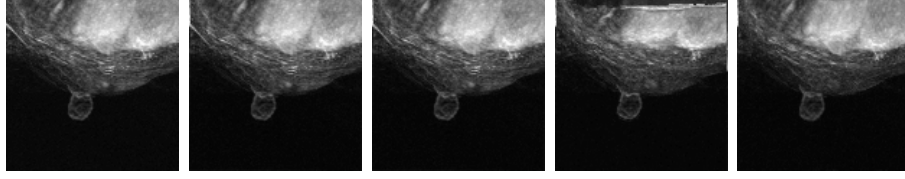


Figure 3.4. A dataset with relatively small amount of motion. In this case, rigid and nonrigid registrations were rated similarly in the subjective tests. From left to right: Maximum Intensity Projection (MIP) subtraction (before registration), MIP subtraction (rigid NMI), MIP subtraction (rigid NMISSD), MIP subtraction (nonrigid NMI), MIP subtraction (nonrigid NMISSD).

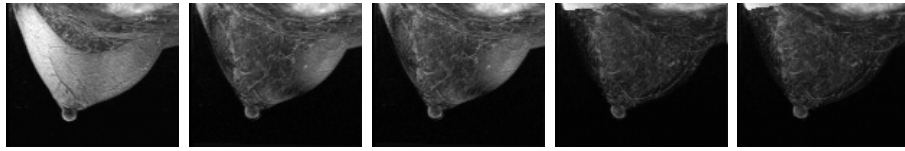


Figure 3.5. A dataset with moderate amount of motion. In this case, nonrigid registration performed clearly better than rigid registration. From left to right: Maximum Intensity Projection (MIP) subtraction (before registration), MIP subtraction (rigid NMI), MIP subtraction (rigid NMISSD), MIP subtraction (nonrigid NMI), MIP subtraction (nonrigid NMISSD).

clearly seen for NMI from the binary mask. Another example, Case 2, is shown in Figure 3.7. This patient has been diagnosed with invasive lobular carcinoma and the lesion is very big. Motion artifact is mostly present at the breast boundary. Rigid registration is not effective in removing this artifact. After nonrigid registration, the artifact at the breast boundary has been removed but at the same time volume reduction is observed.

3.4.3 Computational Complexity

In nonrigid registration, the computational load is extremely heavy due to the exceedingly high degree of freedom. The similarity measure has to be evaluated twice each

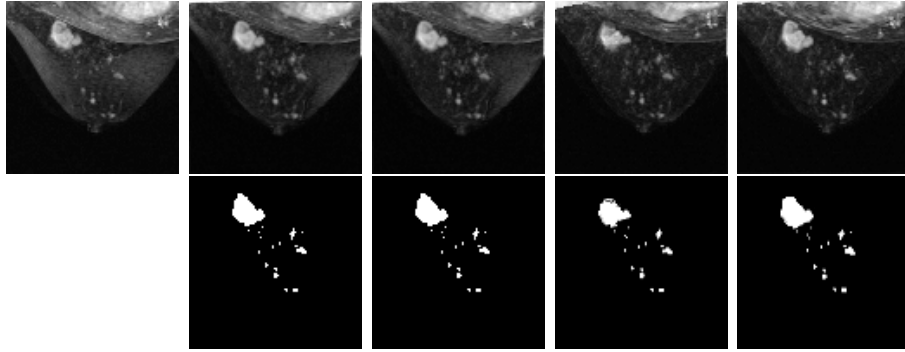


Figure 3.6. Lesion volume test Case 1. Top from left to right: Maximum Intensity Projection (MIP) subtraction (before registration), MIP subtraction (rigid NMI), MIP subtraction (rigid NMISSD), MIP subtraction (nonrigid NMI), MIP subtraction (nonrigid NMISSD). Bottom from left to right: binary lesion masks of the corresponding top row image. Nonrigid registration by NMI has caused the lesion to shrink by 22.63%, while NMISSD has reduced the shrinkage to 2.23%.

time we approximate the gradient in any dimension for a control node. Therefore, the similarity measure has to be computed six times when we optimize one control node in 3D. In this section, we present the results of the timing analysis we have conducted for the proposed method. All the experiments have been carried out on a Pentium IV Dell PC with 3.2GHz processor and 1GB RAM. The average ROI size is about $110 \times 110 \times 26$ voxels. We have taken advantage of the compact local support of B-splines when computing the similarity measure during the optimization process. Linear interpolation has been used to compute the value of the mapped intensities. We have used fixed step gradient descent search in the optimization process, where the magnitude of the gradient has been ignored and only the direction is taken into account. Exactly same parameters have been used in all the experiments except for the choice of similarity measure.

NMI computation is slow because we need to construct the normalized joint histogram each time and compute the sum of the logarithm of each histogram entry. Our

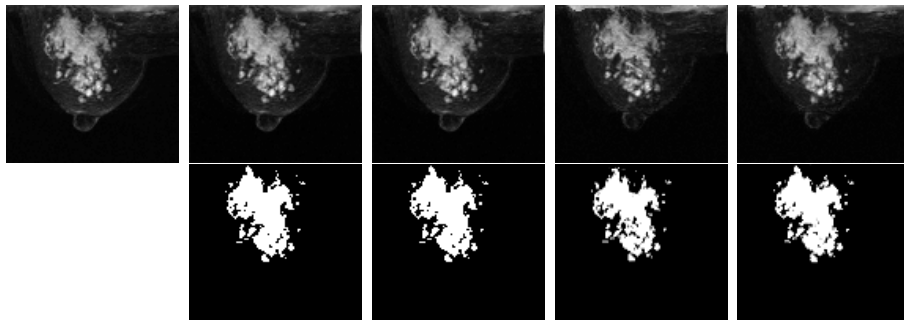


Figure 3.7. Lesion volume test Case 2. Top from left to right: Maximum Intensity Projection (MIP) subtraction (before registration), MIP subtraction (rigid NMI), MIP subtraction (rigid NMISD), MIP subtraction (nonrigid NMI), MIP subtraction (nonrigid NMISD). Bottom from left to right: binary lesion masks of the corresponding top row image. Nonrigid registration by NMI has caused the lesion to shrink by 8.71%, while NMISD has reduced the shrinkage to 3.14%.

method use weighted SSD to approximate the NMI gradient, reducing the running time from NMI by approximately half. The average timing of different registration methods of our test cases are listed in Table 3.2. In actual registration systems, many of the registration parameters like the number of control points, the number of the histogram bins and the learning rate used in optimization need to be tuned for different datasets. Therefore, it is desirable to shorten the registration time so that the user could change the parameters interactively by observing the registration outcome.

3.5 Conclusion

We have designed a nonrigid registration algorithm for CEMRM images in this paper. By the use of auxiliary images constructed from conditional probability distribution of image pairs, we showed that we can approximate the NMI gradient using SSD. Our algorithm attempts to model the distribution of the enhanced intensity for every

Table 3.1. Effect of lesion volume change before and after nonrigid registration. The size of lesion is given in mm^3 and percentage of changes in volume before and after registration by different methods are listed.

Case ID	Lesion Size(mm^3)	NMI	NMI-SSD
1	2397.9	-22.63%	-2.23%
2	13109.4	-8.71%	-3.14%
3	500.3	-1.61%	-0.68%
4	92.1	0.20%	-0.51%
5	1378.1	0.74%	0.12%
6	430.6	-5.40%	-1.47%
7	2341.4	1.42%	-2.04%
8	356.6	-1.55%	-1.88%
Mean \pm Variance	2575.8 \pm 4350.4	-4.69 \pm 8.01%	-1.48 \pm 1.06%

Table 3.2. Registration timing for different methods.

	ROI Size (x, y, z voxels)	NMI (seconds)	NMI-SSD (seconds)
Average	(105, 105, 36)	2467.4	1316.5
Variance	(8, 8, 15)	1182.6	642.6

voxel, so as to take into account the effect of contrast enhancement during registration. Since it is difficult to identify intensity outliers from motion artifacts, it is inevitable that some of the motion artifacts will be considered as lesions. However, we expect the modeling to be good for majority of the voxels, and the registration would be driven by those voxels that are identified correctly. Experiments have confirmed the effectiveness of our algorithm. Our algorithm is able to achieve performance that is close to normalized mutual information but at a much faster speed. It is also shown that our method can effectively prevent misregistration around lesion boundaries, so that physically plausible registration can be obtained.

Chapter 4

A Framework for Registration

Using GPUs

4.1 Introduction

The graphics processing unit (GPU) is a dedicated graphics rendering device found in common personal computers (PCs) and workstations. A GPU implements a number of graphics primitive operations in a way that makes running them much faster than drawing directly to the screen with the host CPU. Their highly parallel structure also makes them more effective than typical CPUs. Modern GPUs have reached a stage where it is possible to use a high-level language to program the shaders to achieve complex rendering effects. Due to the programmability and floating point support available on GPUs, there has been an increasing interest in utilizing it for scientific computing. GPUs employ a *stream* programming model which is distinctively different from the sequential model used by CPUs. The stream programming

model organizes data into parallel streams and computational kernels in the form of fragment programs operate on them.

Image processing applications are particularly suitable for this programming model, because identical localized operations are often applied throughout the entire image. There are several attempts to use GPUs in image processing found in literature. Yang *et al.* [22] made use of a GPU to perform real-time stereo depth calculations. Lefohn *et al.* [23] proposed a 3D level-set solver for fast segmentation on a GPU. Strzodka *et al.* [24] was the first one to make use of GPU to perform registration on 2D images. They implemented a gradient flow registration method on a GPU which resulted in computation time of less than 2 seconds on 256×256 images. They adopted a per-pixel displacement vector field to model the motion between pair of images. Regularized local image gradient information at every pixel was used to perform updates on the displacement vector field.

The degree of freedom of FFD is proportional to the number of control points. In medical applications, the images are 3D and there is a large amount of data to handle. A large number of control points is needed to correct local deformations. Since the position of every control point needs to be optimized independently, the registration process is computationally intensive. In this chapter, we propose a framework for the registration of 3D medical image volumes using GPU. The method is also applicable to processing of images with very high resolutions, e.g., satellite images. The 3D volumetric images are packed into a flat 2D texture for efficient one-pass rendering. The framework makes use of a modified version of the FFD where we have used trilinear interpolation instead of cubic B-spline to compute the displacement of voxels

from the control points. By using trilinear interpolation, we can make use of the hardware accelerated interpolation feature available on GPUs. Our framework is able to incorporate any intensity-based similarity measures such as sum of squared difference (SSD) and normalized correlation coefficient (NCC). In our application, the parallel processing paradigm in GPU programming is fully utilized by packing image data into a data streams in order to optimize the control points efficiently. We perform a thorough analysis of the performance of the system in terms of registration accuracy and registration timing. We demonstrate that significant speed improvement can be obtained without much loss in accuracy.

4.2 Piece-wise Linear Transform and Optimization

We use the formulation in chapter 2. And a piece-wise linear coordinate transformation model that is similar to the cubic B-Spline model found in [7] was used. A regular grid of control points is defined on the image and deformation is achieved by independently moving the control points. Defining the control point position as ϕ_i , where i denotes the index of the control point. The transformation for a voxel with physical coordinates (x, y, z) is given by

$$T(x, y, z) = \sum_n L(d_x)L(d_y)L(d_z)\phi_n \quad (4.1)$$

where ϕ_n denotes the positions of all the control points that are at the corners of the 3D cell containing the voxel (x, y, z) . $L(\cdot)$ denotes the linear interpolator and

$\{d_x, d_y, d_z\}$ are computed as,

$$d_x = \frac{x}{\delta_x} - \lfloor \frac{x}{\delta_x} \rfloor, d_y = \frac{y}{\delta_y} - \lfloor \frac{y}{\delta_y} \rfloor, d_z = \frac{z}{\delta_z} - \lfloor \frac{z}{\delta_z} \rfloor \quad (4.2)$$

where $\{\delta_x, \delta_y, \delta_z\}$ are the intervals between adjacent control points in different coordinate axis directions and $\lfloor \cdot \rfloor$ denotes the floor operation.

To find the best possible transformation $T(\cdot)$, we need to optimize every control point independently. In our applications, we assume that the images have already been brought into coarse alignment by some rigid registration, and thus there are only local differences to be corrected. Therefore, it is usually sufficient to find a local optimum using gradient based optimization techniques. To optimize one control point, we first compute the similarity measure and its gradient, then search for the optimum along the direction of the gradient. This process is iterated until the improvement in image similarity measure falls below a predefined threshold.

We have used finite difference approximation to calculate the gradients of the similarity measure. Therefore, image similarity is to be computed many times when we calculate the gradients in 3D. To compute the similarity measure, every voxel in the moving image is to be warped into the coordinate system of the reference image and interpolation is used to find its mapped intensity value. Since there are so many control points, these steps are repeated many times and this contributes to the major portion of the computational load in nonrigid registration. In the following sections, we will discuss strategies for efficient parallelized computation of the image similarity measure and its gradients.

4.3 GPU Implementation

4.3.1 Basics of GPU Programming

The graphics pipeline is highly optimized for graphics applications. We have shown the flow of its operation in Figure 4.1. When objects need to be drawn, we issue a drawing command via an API such as OpenGL and specify the coordinates of the object vertices. The vertices are passed through the vertex processor and undergo transformations which position the objects at the right geometry. The vertices are then assembled into geometric primitives and then rasterized into fragments, which are further processed by fragment processors before it is finally drawn onto the screen.

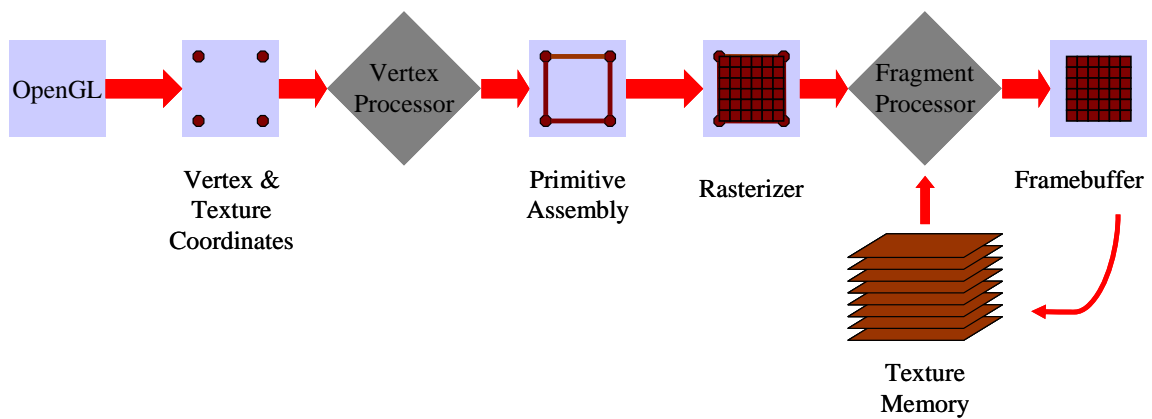


Figure 4.1. The graphics pipeline in latest generation graphics hardware. Programmable vertex and fragment processors provide added flexibility.

The fundamental data storage unit on a GPU is called *texture*, available in one,

two and three dimensions. When viewed from a general purpose programming perspective, they can be considered as equivalent to arrays. The fragment processors are the main computation kernels if GPU is used as a stream processor. When writing a GPU program, we first need to determine the data-parallel portion of the application and code it into fragment program kernels. To invoke a kernel, we specify the range of the computation by rendering a quadrilateral on the image plane, and the region of pixels (and the data contained in it) covered by the quad is sent through the pipeline and passed through the kernels for processing. We can set a texture as a *rendering target*, so that the computed values output from the fragment programs can be saved in a texture for further processing.

4.3.2 GPU-based Registration

Data Storage

Although 3D texture seems to be a natural choice for the storage of 3D medical image volumes, it is not convenient to be used in our nonrigid registration application. This is because we need to warp the 3D moving volume from time to time in order to match the reference volume. Current GPUs do not have support for the writing to a slice of a 3D texture. As an alternative, we have chosen to use *flat 3D textures* proposed by Harris *et al.* [25] for the real-time cloud simulations. As shown in Figure 4.2, the 3D volume is packed into a single flat 2D texture and a scheme which translates the 3D address to 2D address and vice versa is maintained. This scheme can also ensure that the local neighborhood of each slice is packed in the same 2D texture so as to facilitate efficient parallelized computations. Another advantage of using a single 2D

texture instead of a stack of separate 2D textures is that we can invoke the processing of the data using one single rendering pass, instead of multiple rendering passes.

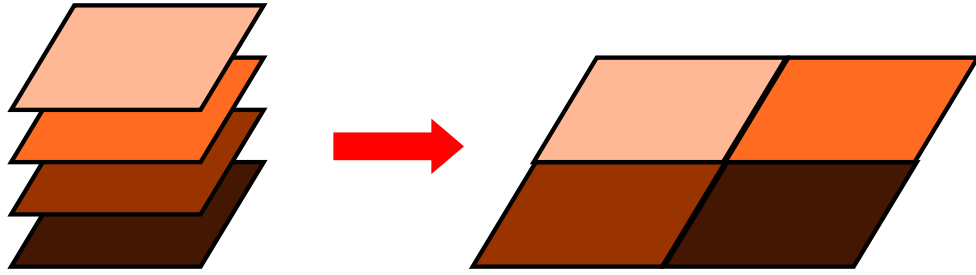


Figure 4.2. Illustration of the data storage scheme. Slices of the 3D volume are packed into a single 2D flat texture.

Transforming the Image

We store the positions of the control points ϕ_i in 2D flat textures as well, but with a reduced resolution as compared to the original image volume. In each rendering pass, we know the exact coordinates of every voxel in the 2D flat texture. It is possible to fetch the position of the control points nearest to the voxel (or *fragment* in terms of graphics terminology) via texture lookup operation. This process is exactly the same for every voxel and therefore we can exploit the Single Instruction Multiple Data (SIMD) architecture on GPUs to perform it in parallel. The computational kernel is implemented using a fragment shader. The steps performed in the kernel for every fragment can be summarized as:

1. Calculate the indices of the neighbor control points from the current fragment

coordinate.

2. Fetch the location of the control points using texture lookups.
3. Interpolate the displacement for the current voxel from the control points.

Computation of Global Similarity Measure

The global similarity measure is calculated using the warped image and the reference image. Two steps are performed to complete this task. The terms inside the summation in (2.14) is first computed using a simple fragment shader which performs voxel-wise operations. The results are stored in a rendered texture which need to be summed up. We perform summation of these individual values via a process known as the *reduce* operation, which can be achieved by alternately rendering a pair of textures, each time reducing the dimension of the rendering target by half and summing up the neighboring 4 fragments. This process is repeated until the dimension of the output texture is reduced to 1×1 . For a texture of size n , $O(\log(n))$ operations are needed as compared to sequential processing of $O(n)$ operations on a CPU. The process of summing up similarity measure is illustrated in Figure 4.3.

Localized Gradient Computation

We have used finite difference approximation to compute the gradient of the similarity measure. The control points are perturbed in the positive and negative directions respectively and the gradient of the similarity measure is computed based on the two sets of images. If we denote the function which computes the similarity measure by $f(\cdot)$, the x - coordinate of the control point being optimized by \mathbf{p}_x , the gradient in

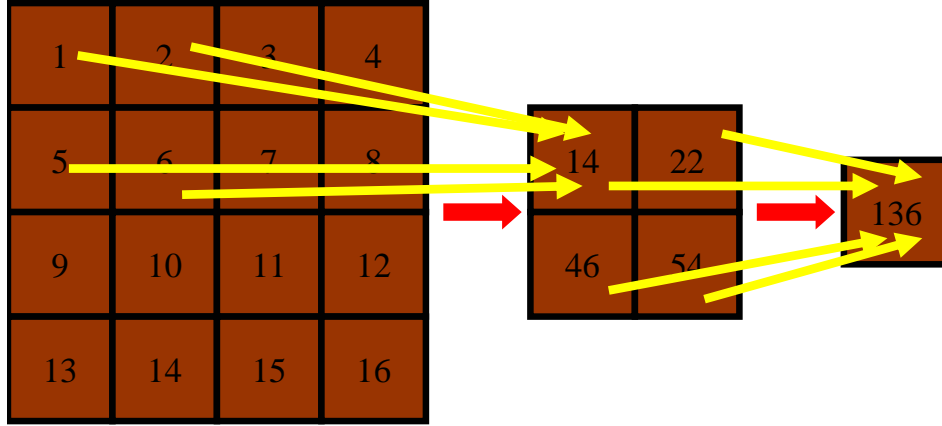


Figure 4.3. The reduce operation to sum up the values in a texture.

the x -direction by $\nabla_x f$, and the small perturbation by ϵ , the gradient is computed as,

$$\nabla_x f = \frac{f(\mathbf{p}_x + \epsilon) - f(\mathbf{p}_x - \epsilon)}{2\epsilon} \quad (4.3)$$

Since the transformation model we used is piece-wise linear, moving a particular control point only affect the mapping of the voxels in its immediate neighborhood. The support of every control point is defined by a linear interpolation kernel. Therefore, the effect of the small perturbation is negligible in the regions near to neighboring control points, and the effect is zero for regions beyond that. We can exploit this fact to compute $f(\mathbf{p}_x + \epsilon)$ and $f(\mathbf{p}_x - \epsilon)$ simultaneously for alternate control points. An illustration of this idea is shown in Figure 4.4.

The simultaneous computation of $f(\mathbf{p}_x + \epsilon)$ and $f(\mathbf{p}_x - \epsilon)$ for alternate control points can be achieved by perturbing alternate control points appropriately and ren-

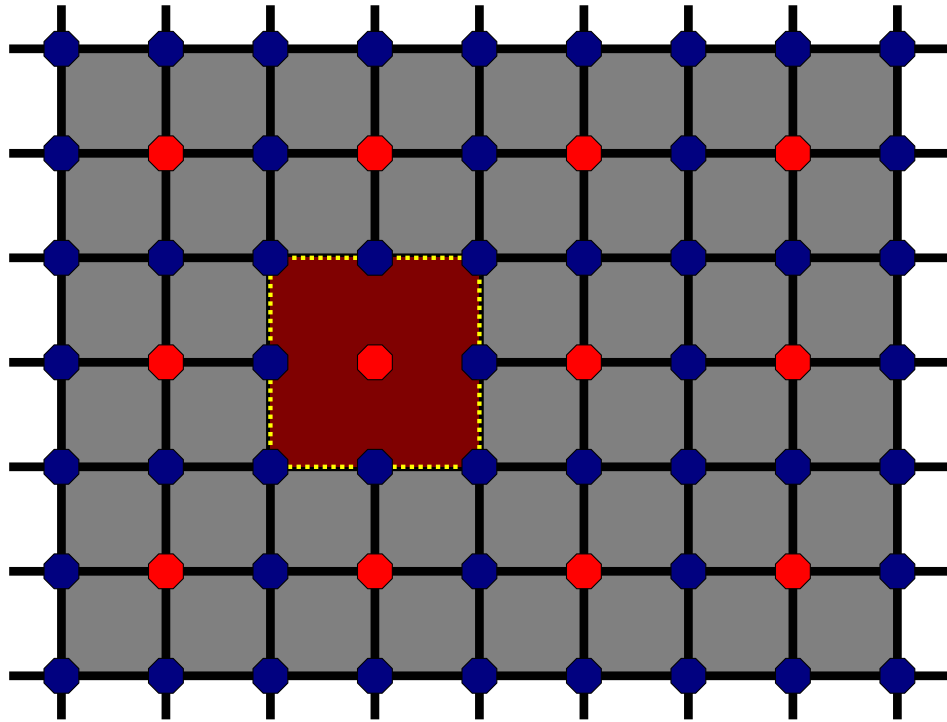


Figure 4.4. 2D illustration of the localized support of each control point. The points marked red are positioned alternately on the control point grid, and therefore the similarity measure gradients can be computed simultaneously for them. The region of support is also shown for one of the control point.

der the entire image two times and compute its difference. In order to aggregate the measure, we still need to apply the texture reduce operation. However, instead of reducing the texture size to 1×1 as in global similarity calculation, we reduce the texture only to the size that is the same as the number of control points that we want to compute its gradient. In this way, we will have a texture in which every single pixel contains the gradient value of its corresponding control point. To compute similarity gradients for other control points, we simply shift the entire image texture by an amount equal to the control point interval and the same computation kernel can be applied.

Registration System

To this end, we have described all the individual kernels that are necessary for the computation of several important components in the registration process. We are now ready to describe the flow of our registration system on the GPU. For every iteration, we perturb the control points in a CPU program and load the control point positions into the GPU memory. The image is warped using the control points and gradients calculated on the GPU. At the end of an iteration, the control points positions are updated on the CPU using the computed gradients. The steps taken can be summarized as follows:

1. Transform the moving image using the image transform kernel (GPU accelerated).
2. Calculate the gradient for every control point (GPU accelerated).
3. Compute the global similarity measure (GPU accelerated).

4. If the change in global similarity measure is smaller than a predefined threshold, the process is terminated. Otherwise, update the control points using the gradient descent rule, low pass filter the updated positions, and go to Step 1 (On CPU).

The major portion of the computation process has been offloaded to the GPU in order to make full use of its hardware acceleration capability. The control point update step performed on the CPU is computationally efficient due to the simplicity of the operation. We have chosen to low pass filter the control point positions so as to introduce some correlations into adjacent control points. By doing so, the transformation defined by the control points will become smoother.

4.4 Experiments and Results

We have used the same datasets from our study of contrast-enhanced breast MR imaging to test the effectiveness of our method. Here we just restate the protocol for completeness. Image acquisition was done using a GE Sigma 1.5 Tesla coil MRI scanner with 3-D fast-spoiled gradient echo and no spectral fat suppression ($TR = 25.6\text{ms}$, $TE = 3\text{ms}$, fractional echo, Flip angle = 30° , $FOV = 32$ to 40cm). The contrast agent used was Magnevist Gd-DTPA of concentration 0.2mmol/kg . A typical dataset has 5 scans ($256 \times 256 \times 24$ voxels) of voxel size $1.05\text{mm} \times 1.05\text{mm} \times 5.45\text{mm}$. Slice direction used is axial. Variations to this protocol are mainly in the number of slices, which can vary from 16 to 56 depending on the volume size to be acquired. The contrast agent is injected after the first scan, and post-contrast scans will follow in

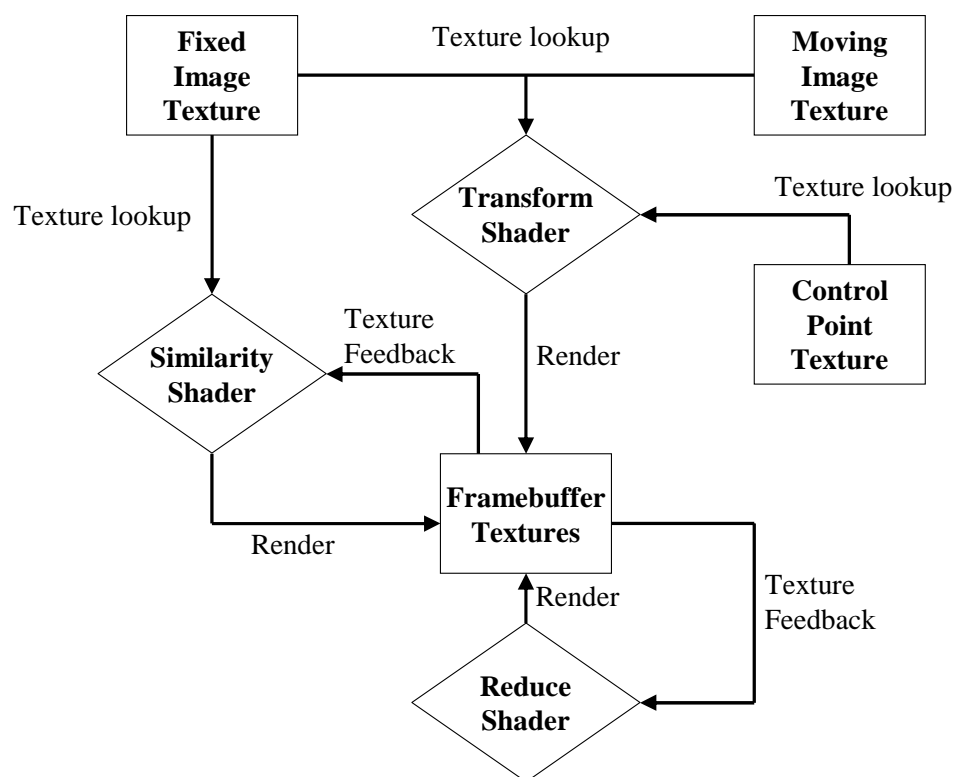


Figure 4.5. Block diagram of the GPU registration system.

the next 5 to 20 minutes. Each 3-D scan requires 30-60 seconds of acquisition time, depending on the number of slices.

We tested our registration system using an NVIDIA GeForce 7800 graphics processing unit which has 512MB onboard memory. The registration system was implemented using Cg (C for graphics) and OpenGL. The CPU portion of the application was implemented using C++.

Extensive experiments have been conducted to verify our registration system. First, we investigate the effect of varying the number of control points on the final registration results. We then proceed to test the algorithm implementation using more datasets. Lastly, we run simulations to give an analysis of the timing of this implementation.

4.4.1 Selection of Control Point Resolution

With the low pass filtering of the control point positions, the transformation defined by the control points should be smooth and approximates a spline if the number of points is large. In this section, we summarize results for the experiments on varying the resolution of the control point mesh and the study of how it affects registration. We used a dataset without lesions having an initial Sum of Squared Difference (SSD) of 79.10 before registration. The size of the image Region of Interest (ROI) is $(100 \times 100 \times 28)$.

Starting from low resolution in all dimensions, we systematically increased the number of control points and calculate the difference of the registered image and the reference image. Since cubic B-splines have been successfully applied and validated

in nonrigid registration [7], we also registered the images using splines with an implementation based on the Insight Toolkit [26]. The number of control points used for spline registration is $(8 \times 8 \times 8)$. The SSD value after spline registration is 16.24. We then compared the images registered using our algorithm with the images registered using cubic B-splines and calculate the difference. The results have been summarized in Table 4.1.

Table 4.1. Effect of varying control point resolution on the registration results.

Control Point Resolution	SSD before registration	SSD with reference image after registration	SSD with B-spline image after registration
$4 \times 4 \times 7$	79.10	29.83	18.53
$8 \times 8 \times 7$	79.10	23.43	14.55
$16 \times 16 \times 7$	79.10	21.75	14.53
$16 \times 16 \times 14$	79.10	21.03	13.77
$32 \times 32 \times 14$	79.10	19.78	15.01
$64 \times 64 \times 14$	79.10	23.67	19.32

It can be inferred from the results that with increasing control point resolution, we are generally able to obtain better registration because finer motion can be modeled by a denser control point mesh. However, we have also observed that increased number of control points does not guarantee low SSD value after registration. We can see from the results that when the control point mesh resolution reaches $(64 \times 64 \times 14)$, the SSD value after registration has increased. This is because of the fact that every control point has a localized support. If the number of control points is high, each control point would have a very small region of influence, and this would increase the chance of terminating the registration in a local minimum. We have also calculated the difference of the images registered using our method to the images registered using B-splines. The difference decreased with increasing control point resolution.

Similarly, the difference also increased slightly when the control points are too dense. However, the difference are generally quite small and this shows that our method by linear interpolation is consistent with Spline-based registration.

4.4.2 Registration Result on More Datasets

In this section, we perform some experiments on datasets that contain lesions which are enhanced in intensity after the injection of contrast agent. The registration algorithm is based on [18][19]. The normalized mutual information (NMI) criterion has been approximated by a combination of two SSD terms, which are computed between original images and auxiliary images created from the voxel conditional probability distributions. We have implemented the algorithm on a GPU.

Some result images are shown in Figure 4.6 and Figure 4.7. As we can see from the images. The registration worked well in terms of artifact reduction. Most of the motion artifacts have been removed after registration. We are able to better visualize the lesions after registration. In terms of running time, the unoptimized CPU implementation based on ITK requires 15 to 30 minutes depending on the size of the image to be registered. For GPU implementation, the running time is cut down to generally less than 1 minute. Substantial speed up has been obtained.

4.4.3 Analysis of Running Time

In this section, we describe results of the timing analysis of our GPU implementation. We first describe the relationship of the total running time with respect to the number of control points. A image volume ROI pair of size $100 \times 100 \times 28$ is used in this

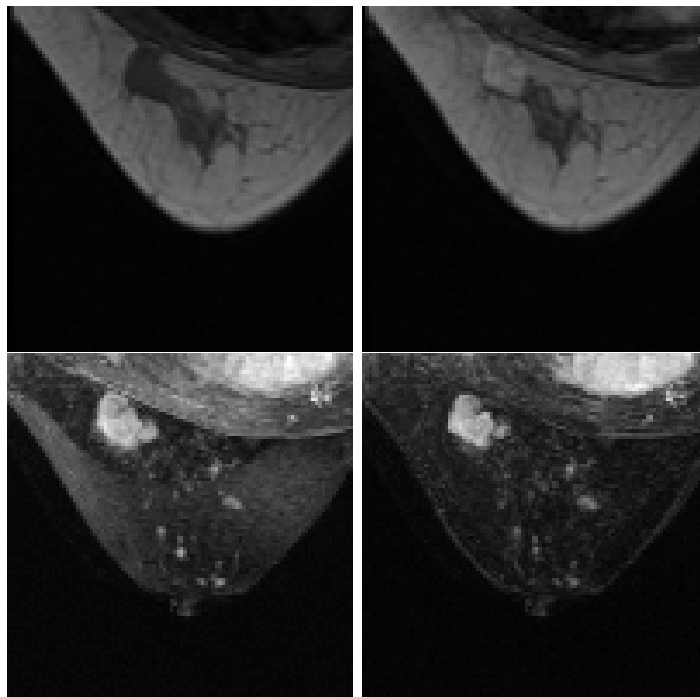


Figure 4.6. Top left: Pre-contrast image. Top right: Post-contrast image. Bottom left: Maximum Intensity Projection (MIP) of the difference image before registration. Bottom right: MIP after GPGPU registration.

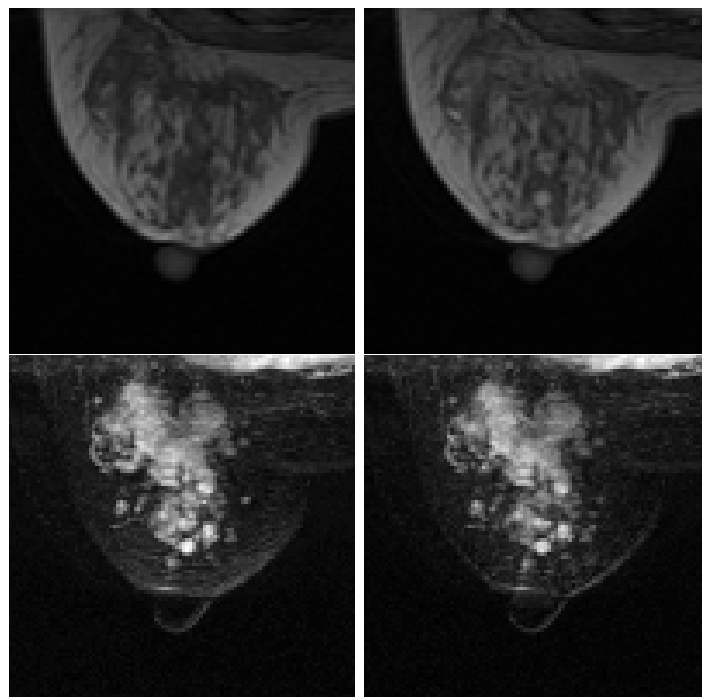


Figure 4.7. Top left: Pre-contrast image. Top right: Post-contrast image. Bottom left: Maximum Intensity Projection (MIP) of the difference image before registration. Bottom right: MIP after GPGPU registration.

experiment. We tested different number of control points and run the registration algorithm for 100 iterations each time in order to have a fair comparison. The results have been summarized in Table 4.2. We can see that the timing is approximately constant for control point resolutions from $4 \times 4 \times 7$ to $16 \times 16 \times 14$. For CPU implementation, we would have expected the running time to increase linearly with the number of control points. However, due to the SIMD architecture and the parallel processing capability of GPU, the running time does not really increase with the number of control points. However, when the number of control points is greater than what the GPU can handle in parallel, the running time would increase. Exactly when the running time will increase depends on the capability of the GPU, for our case, it is $64 \times 64 \times 14$. Combining with the analysis given in Section 4.4.1, we are able to determine the most feasible number of control points by considering the tradeoff.

We next examine the relationship of the running time with respect to the size of the images to be registered. We run the algorithm on image sets with different sizes and record their running time. The number of control points have been fixed at $32 \times 32 \times 14$. Similar to the previous experiment, we run the algorithm for 100 iterations for comparison. The results have been summarized in Table 4.3 and Figure 4.8. It can be seen that the running time increases linearly with the size of the image in terms of total number of image voxels.

Table 4.2. Effect of varying control point resolution on the registration results.

Control Point Resolution	Time (sec)
$4 \times 4 \times 7$	51.78
$8 \times 8 \times 7$	50.20
$16 \times 16 \times 7$	48.93
$16 \times 16 \times 14$	51.13
$32 \times 32 \times 14$	56.03
$64 \times 64 \times 14$	80.34

Table 4.3. Running time analysis for different image sizes.

Image Volume Resolution	Total size (Voxels)	Time (Sec)
$128 \times 128 \times 28$	458752	30.20
$156 \times 156 \times 28$	681408	40.65
$184 \times 184 \times 28$	947968	52.28
$212 \times 212 \times 28$	1258432	65.45
$240 \times 240 \times 28$	1612800	81.54

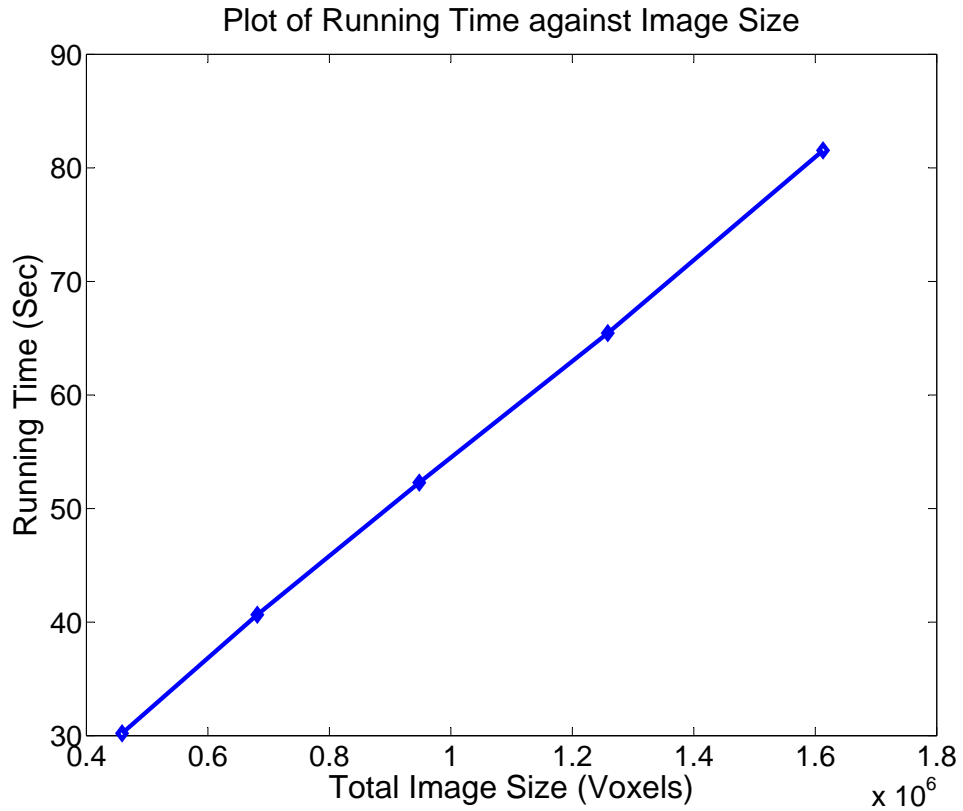


Figure 4.8. Plot of running time in seconds against the image size.

Chapter 5

Conclusion

In this work, we showed it is possible to obtain fast approximation of the gradient of normalized mutual information cost function using sum of squared difference between auxiliary images and original images. We created the auxiliary images by modeling the conditional probability density function as a mixture of Gaussians, each representing the inliers (normal structures) and the outliers (enhanced structures). The approximation resulted in 50% reduction of the optimization time. The registration quality is similar compared to the direct use of NMI gradient in optimization. By modeling the outliers explicitly, it was also shown that the volume of the contrast enhanced structures can be preserved.

We have also proposed a framework for 3D medical image registration using intensity-based similarity measures on commodity GPUs. We have tested our implementation on contrast-enhanced breast MR images. The results have shown that our method is able to remove most of the motion artifacts, allowing for better visualization of breast lesions. The timing can be generally controlled to below 1 minute,

offering substantial speedup to common CPU implementations. Since off-the-shelf commodity GPUs are cheap, this makes our method an attractive choice in cost-effective medical applications.

Appendix A

Derivation of NMI gradient

The expression of normalized mutual information is given by

$$\text{NMI}(u, v) = \frac{H(u) + H(v)}{H(u, v)} \quad (\text{A.1})$$

To calculate its derivative with respect to a transformation parameter ϕ , we invoke the quotient rule:

$$\begin{aligned} \frac{\partial \text{NMI}(u, v)}{\partial \phi} &= \frac{1}{H^2(u, v)} \left[\left(\frac{\partial H(u)}{\partial \phi} + \frac{\partial H(v)}{\partial \phi} \right) H(u, v) - \frac{\partial H(u, v)}{\partial \phi} (H(u) + H(v)) \right] \\ &= \frac{1}{H(u, v)} \left[\frac{\partial (H(u) + H(v))}{\partial \phi} - \text{NMI}(u, v) \frac{\partial H(u, v)}{\partial \phi} \right] \end{aligned} \quad (\text{A.2})$$

We assume that $H(u)$ is approximately invariant to the transformation if the image overlap does not change, therefore $\frac{\partial H(u)}{\partial \phi} = 0$. Hence,

$$\begin{aligned}
\frac{\partial \text{NMI}(u, v)}{\partial \phi} &\simeq \frac{1}{H(u, v)} \left[\frac{\partial H(v)}{\partial \phi} - \text{NMI}(u, v) \frac{\partial H(u, v)}{\partial \phi} \right] \\
&= \frac{1}{H(u, v)} \left[\frac{\partial H(u, v) - H(u|v)}{\partial \phi} - \text{NMI}(u, v) \frac{\partial H(u, v)}{\partial \phi} \right] \\
&= \frac{1}{H(u, v)} \left[(1 - \text{NMI}(u, v)) \frac{\partial H(u, v)}{\partial \phi} - \frac{\partial H(u|v)}{\partial \phi} \right] \\
&= \frac{1}{H(u, v)} \left[(1 - \text{NMI}(u, v)) \frac{\partial H(u) + H(v|u)}{\partial \phi} - \frac{\partial H(u|v)}{\partial \phi} \right] \\
&= \frac{1}{H(u, v)} \left[(1 - \text{NMI}(u, v)) \frac{\partial H(v|u)}{\partial \phi} - \frac{\partial H(u|v)}{\partial \phi} \right] \tag{A.3}
\end{aligned}$$

Using the fact that $1 - \text{NMI}(u, v) = \frac{H(u, v) - H(u) - H(v)}{H(u, v)}$ and $\text{MI}(u, v) = H(u) + H(v) - H(u, v)$, we can further rewrite (A.2) as

$$\frac{\partial \text{NMI}(u, v)}{\partial \phi} = \frac{1}{H^2(u, v)} \left[-\text{MI}(u, v) \frac{\partial H(v|u)}{\partial \phi} - H(u, v) \frac{\partial H(u|v)}{\partial \phi} \right] \tag{A.4}$$

Bibliography

- [1] A. Jackson, D. L. Buckley, and G. J. M. Parker. *Dynamic Contrast-Enhanced Magnetic Resonance Imaging in Oncology*. Springer, 2005.
- [2] S. C. Wang. Magnetic resonance imaging of the breast. *Gynecologic Imaging*, John C. Anderson. Churchill Livingstone.
- [3] T. Rohlfing and C. R. Maurer Jr. Nonrigid image registration in shared-memory multiprocessor environments with application to brains, breasts, and bees. *IEEE Transactions on Information Technology in Biomedicine*, 7(1):16–25, 2003.
- [4] P. Hayton, J. M. Brady, L. Tarassenko, and N. Moore. Analysis of dynamic mr breast images using a model of contrast enhancement. *Medical Image Analysis*, 1(3):207–224, 1996.
- [5] T. Rohlfing, C. Maurer Jr., D. A. Bluemke, and M. A. Jacobs. Volume-preserving non-rigid registration of mr breast images using free-form deformation with an incompressibility constraint. *IEEE Transactions on Medical Imaging*, 22(6):730–741, 2003.
- [6] C. Tanner, J. A. Schnabel, D. Chung, M. J. Clarkson, D. Rueckert, D. L. G. Hill, and D. J. Hawkes. Volume and shape preservation of enhancing lesions when applying non-rigid registration to a time series of contrast enhancing mr breast images. In *Medical Image Computing and Computer-Assisted Intervention*, pages 327–337, 2000.
- [7] D. Rueckert, L. I. Sonoda, C. Hayes, D. L. G. Hill, M. O. Leach, and D. J. Hawkes. Nonrigid registration using free-form deformations: Application to breast mr images. *IEEE Transactions on Medical Imaging*, 18(8), August 1999.

-
- [8] A. Collignon, F. Maes, D. Delaere, D. Vandermeulen, P. Suetens, and G. Marchal. Automated multi-modality image registration based on information theory. In *Information Processing in Medical Imaging*, pages 263–274, Norwell, MA: Kluwer, 1995.
 - [9] P. Viola and W. M. Wells III. Alignment by maximization of mutual information. In *International Conference on Computer Vision*, Boston, MA, June 1995.
 - [10] C. Studholme, D. L. G. Hill, and D. J. Hawkes. An overlap invariant entropy measure of 3d medical image alignment. *Pattern Recognition*, 32(1):71–86, 1999.
 - [11] T. Rohlfing, C. Maurer Jr., D. A. Bluemke, and M. A. Jacobs. An alternating-constraints algorithm for volume-preserving non-rigid registration of contrast-enhanced mr breast images. In *Workshop on Biomedical Image Registration*, pages 291–300, 2003.
 - [12] E. Haber and J. Modersitzki. Numerical methods for volume preserving image registration. *Inverse Problems*, 20:1621–1638, 2004.
 - [13] X. H. Chen, M. Brady, J. L.-C. Lo, and N. Moore. Simultaneous segmentation and registration of contrast-enhanced breast mri. In *IPMI*, pages 126–137, 2005.
 - [14] C. Tanner, J. A. Schnabel, A. Degenhard, A. D. C.-Smith, C. Hayes, M. O. Leach, D. R. Hose, D. L. G. Hill, and D. J. Hawkes. Validation of volume-preserving non-rigid registration: Application to contrast-enhanced mr-mammography. In *MICCAI (1)*, pages 307–314, 2002.
 - [15] F. Maes, D. Vandermeulen, and P. Suetens. Comparative evaluation of multiresolution optimization strategies for multimodality image registration by maximization of mutual information. *Medical Image Analysis*, 3(4):373–386, 1999.
 - [16] P. Thévenaz and M. Unser. Optimization of mutual information for multiresolution image registration. *IEEE Transactions on Image Processing*, 9(12):2083–2099, 2000.
 - [17] W. Wells, P. Viola, H. Atsumi, S. Nakajima, and R. Kikinis. Multi-modal volume registration by maximization of mutual information. *Medical Image Analysis*, 1(1):35–51, 1996.
 - [18] Y. Sun, C. H. Yan, S. H. Ong, E. T. Tan, and S.-C. Wang. Intensity-based volumetric registration of contrast-enhanced mr breast images. In *MICCAI (1)*, pages 671–678, 2006.

- [19] Y. Sun, S. H. Ong, S.-C. Wang, E. T. Tan, and C. H. Yan. Volume-preserving registration of dynamic contrast-enhanced breast mr images. *IEEE Transactions on Medical Imaging*, submitted.
- [20] M. Leventon and W. Grimson. Multi-modal volume registration using joint intensity distributions. In *Medical Image Computing and Computer-Assisted Intervention*, pages 1057–1066, 1998.
- [21] A. Roche, G. Malandain, X. Pennec, and N. Ayache. The correlation ratio as a new similarity measure for multimodal image registration. In *Medical Image Computing and Computer-Assisted Intervention*, pages 1115–1124, 1998.
- [22] R. G. Yang and M. Pollefeys. A versatile stereo implementation on commodity graphics hardware. *Real-Time Imaging*, 11(1):7–18, 2005.
- [23] A. E. Lefohn, J. M. Kniss, C. D. Hansen, and R. T. Whitaker. A streaming narrow-band algorithm: Interactive computation and visualization of level sets. *IEEE Trans. Vis. Comput. Graph.*, 10(4):422–433, 2004.
- [24] R. Strzodka, M. Droske, and M. Rumpf. Image registration by a regularized gradient flow. a streaming implementation in dx9 graphics hardware. *Computing*, 73(4):373–389, 2004.
- [25] M. J. Harris, W. V. Baxter, T. Scheuermann, and A. Lastra. Simulation of cloud dynamics on graphics hardware. In *HWWS '03: Proceedings of the ACM SIGGRAPH/EUROGRAPHICS conference on Graphics hardware*, pages 92–101, Aire-la-Ville, Switzerland, Switzerland, 2003. Eurographics Association.
- [26] InsightToolkit. <http://www.itk.org>.